TRIPLE-SHAPE COEXISTENCE AND SUPERDEFORMATION IN Pb ISOTOPES

Tabassum Naz

Department of Physics, Aligarh Muslim University Aligarh, India

Shakeb Ahmad

Physics Section, Women's College, Aligarh Muslim University Aligarh, India

H. Abusara

Department of Physics, Birzeit University, Birzeit, Palestine

(Received March 14, 2018; accepted May 6, 2018)

Triple-shape coexistence and superdeformation in Pb isotopes with neutron numbers $N = 96$–138 is studied. The constrained calculations are performed within the Relativistic Hartree–Bogoliubov (RHB) model using DD-ME2, DD-PC1, and NL3* force parameters, and pairing interaction separable in momentum space. Triple-shape coexistence (spherical, prolate and oblate) manifests themselves in a clear manner in $^{184-190}$Pb nuclei with axial RHB calculations. Triaxial RHB calculations further confirm the findings. Superdeformed minimum is observed for $^{188-220}$Pb isotopes, and the corresponding excitation energy, deformation and depth of well are comparable within different force parameters used. The behaviour with neutron number of the superdeformed excitation energy, two-neutron separation energy in the ground state and superdeformed minimum, and its differential are fairly reproducing the trend of the available experimental data. The present numerical results are compared with Macro–microscopic Finite Range Droplet Model (FRDM) and Hartree–Fock–Bogoliubov (HFB) model based on the interaction Gogny-D1S force. Overall, a fairly satisfactory agreement is found within the different force parameters and the calculated and experimental results.

DOI:10.5506/APhysPolB.49.1653

1. Introduction

Recent experimental attempts devoted to understanding the atomic nuclear structure has observed a rich variety of nuclear shapes and structural phenomena. These observations have given a boost for new experiments

as well as how challenges for the theoretical models in the field of nuclear structure research. The different shapes of an atomic nucleus from spherical to some higher order multipole deformations are effectively due to, as now, only a few protons and neutrons are being rearranged among the orbitals around the Fermi surface. In the nuclear structure studies, shape coexistence and shape-phase transitions in nuclei have been a matter of major theoretical and experimental interest for many years. The phenomena of shape coexistence and phase transition along an isotopic and isotonic chain are effectively the outcome of the sensitive correlations between the single particle energies and the collective degrees of freedom [1]. Observations of shape coexistence close to the region around proton $Z = 82$ and neutron $N = 126$ magic numbers of the nuclear chart have been for many years one of the dedicated regions of active nuclear research, both experimentally and theoretically to understand the intrinsic structure of many excitations and their structural evolution. Studies have shown that the shape coexistence at and near the regions of the shell closure is the result from intruder excitations [2, 3], and its origin, in general, is due to the interplay between the neutron–proton interaction and the shell effects [4].

In even–even nuclei, the phenomenon of shape coexistence is interpreted when low-lying 0^+ states with similar energies show different intrinsic deformations. This leads to competing minima close in excitation energy. The experimental observations of several 0^+ states coexisting at low excitation energy are interpreted as coexistence of nuclear shapes [2, 3, 5–11]. It has been supported by many direct evidences such as α-decay studies, in-band and out-of-band γ-ray transition probabilities, measurements of g-factor, and by charge radii [9, 12–18]. Rapid evolution of nuclear structure with neutrons and protons is known in the neutron-deficient Pb region. In the structural interpretation of neutron-deficient Pb nuclei close to the neutron midshell ($N = 104$), experimental observations of collective bands have provided the evidence for shape coexistence. Theoretically, the overall combined effect of the presence of a strong proton shell closure at $Z = 82$ and a large number of neutron holes below $N = 126$ is responsible for the coexistence of the low-lying excited 0^+ states. From the experimental observations of the low-energy spectrum of Pb isotopes around $N = 104$, it is evident that the ground state for all isotopes is predominantly spherical [10, 11]. Coexisting structures with different properties associated with the observation of two lowest excited 0^+ states have been interpreted as an oblate (lower in energy above ^{188}Pb) and a prolate (lower in energy in lighter Pb nuclei) shape. The interesting one is ^{186}Pb with unique excitation spectrum having the three lowest excited 0^+ states [13]. The two 0^+ excited states being located at low excitation energy around 600 keV, associated with two different structures, prolate and oblate, together with the spherical ground state, give evidence for triple-shape coexistence in ^{186}Pb.

Many experiments, through several experimental techniques, have provided the structural richness for neutron-deficient Pb nuclei [6, 9, 13, 19–35]. Collective yrast bands have been identified in the four even–even isotopes $^{182-188}$Pb [21–25]. However, observation of a non-yrast collective band built on the coexisting oblate minimum has been reported in ^{186,188}Pb nuclei [26–32] based on recoil-tagging measurements. In addition to the lowest 0_2^+ (532 keV) state in ^{186}Pb nucleus [36], a systematic lowering of the first excited 0^+ state in the even–even $^{188-202}$Pb isotopes has been observed, where a low-spin sequence of non-yrast states in ^{196}Pb described as a shell-model intruder excitation provides the evidence for the microscopic nature of these states [37]. Recent experimental studies using the total absorption technique at the ISOLDE (CERN) facility have inferred spherical ground states for ^{192,190}Pb isotopes [35].

Coexistence of 0^+ states in Pb isotopes has been extensively studied theoretically [38–59]. In the Nilsson framework, including shell corrections, shape coexistence was predicted in Pb isotopes [38]. The two excited states of Pb nuclei with neutron number close to $N = 104$ were predicted as oblate and prolate in the phenomenological deformed mean-field models and the Strutinsky method based on the yrast line formed by a collective band associated with the prolate minimum, near the ground state spherical configuration [39–43]. The self-consistent mean-field calculations, including correlations beyond the mean field focusing on the static potential energy surface properties of Pb isotopes including its spectroscopic properties account for the coexistence of low-lying excited 0^+ states [45–51]. This has also been studied in the framework of the interacting boson model [52–54]. Besides, a configuration mixing calculations of angular-momentum projected mean-field states using the Skyrme interaction have been performed for neutron deficient Pb nuclei. In the configuration-mixing interacting boson model (IBM), for Pb isotopes, the mid-shell ^{186}Pb has been reported to have three minima (spherical, oblate, and prolate shapes). Moreover, in the heavier Pb isotopes, away from the mid-shell, spherical ground state is found [55]. Recently, an investigation of shape-coexisting rotational states in $^{186-194}$Pb nuclei has been carried out by using angular-momentum-conserved PES calculations [57] which incorporate the Angular-Momentum-Projection (AMP) technique into the macroscopic–microscopic (MM) model [58].

Superdeformation (SD) in Pb isotopes is also one of the interesting features of nuclear structure studies. Nuclear structure experimentalists and theorists over the past two decades have observed several rotational bands corresponding to superdeformed shapes in the $A \sim 150$ and 190 regions [60]. Besides the availability of large amount of experimental information on SD bands, many fundamental properties such as the spin, parities and the excitation energies have not yet been significantly measured [61–66]. The reason behind this is the difficulty to identify the low intensity discrete transitions which links the SD levels to the normal deformed (ND) levels.

In 1989, identification of γ rays comes up with the first experimental evidence for superdeformed (SD) rotational band in ^{191}Hg [66, 67]. Until now, over 85 SD bands have been identified in 25 isotopes with $79 < Z < 84$ in the $A \sim 190$ region. Some of the experimentally identified SD bands in this region are in ^{190,192,194}Hg [61, 62, 68, 69] and ^{190,192,194,195,196}Pb [63–65, 70–72] isotopes. The existence of superdeformed states and their fundamental properties has been predicted within the different theoretical approaches. These approaches include the Strutinsky method with a Woods–Saxon potential [73], the Hartree–Fock–Bogoliubov (HFB) model with different Skyrme forces [74–76], with a Gogny force [77], the cluster model [78], and the relativistic mean-field (RMF) theory [79–81]. These models have predicted exactly the excitation energies and well depth of SD states. Other theoretical calculations have predicted some other interesting features beside the existence of the lowest SD bands, like octupole correlations in the SD minimum, and the existence of low-lying multi-quasiparticle states within the SD minimum [82–88].

Recent observations and predictions, through experimental analysis and theoretical studies on the co-existence of excited 0^+ states below 1 MeV in even–even Pb isotopes between $A = 182$ and $A = 194$, especially the case of triple-shape coexistence, and the prediction that $N = 108$ [71–74] will mark the limit of observable superdeformation (SD) in the Pb isotopes, have motivated us to reanalyse the geometry of even–even Pb isotopes. In the present analysis, we shall present the numerical results of a systematic calculation in the search of ground state properties, shape coexistence, and the structure of the superdeformed state of neutron-deficient isotopes $^{178-220}$Pb with neutron number $N = 96$–138. The systematic constrained axial and triaxial calculation is done in the self-consistent mean-field model — the Relativistic Hartree–Bogoliubov (RHB) with density-dependent zero and finite range N–N interactions. The triaxial calculation is done for those isotopes where the existence of triple-shape coexistence is expected. The model parameters used are: the density-dependent DD-ME2 [89], point-coupling DD-PC1 [90], and non-linear meson-exchange coupling NL3* [91]. They provide a successful description of ground state properties [92–95] over the whole nuclear chart. Pairing correlations are considered in the separable pairing model [96]. A systematic comparison is made with calculated values and experimental data [97, 98], Macro–microscopic Finite Range Droplet Model (FRDM) [99], and self-consistent Hartree–Fock–Bogoliubov (HFB) theory extended by the generator coordinate method and mapped onto a five-dimensional collective quadrupole Hamiltonian (CHBF+5DCH) based on the Gogny-D1S interaction [100]. In the present study, our intention is to get a deeper understanding about density functionals in general. The present study also deals with the superdeformation within RHB not done earlier.

This manuscript is organized as follows. In Section 2, a general overview of the Relativistic Hartree–Bogoliubov (RHB) formalism is presented. In Section 3.1, the numerical results of the calculations are discussed and compared with the results from other works. Summary and conclusions are in Section 4.

2. Theoretical framework

The present investigation is carried out in the framework of covariant density functional theory (CDFT). We use the covariant energy density functionals (CEDFs) based on the finite interaction range DD-ME2 [89], a zero-range point-coupling DD-PC1 [90], and non-linear meson–nucleon coupling (NL3*) [91]. The pairing correlations are treated suitably within the separable pairing model. We have used these models very successfully and have provided an excellent predictions of different ground states and excited state properties [101–104]

2.1. The meson-exchange model

The meson-exchange model is defined by the standard Lagrangian density with medium-dependent vertices [105]

$$\begin{aligned}\mathcal{L} \;=\; & \bar{\psi}\left[\gamma(i\partial - g_\omega\omega - g_\rho\vec{\rho}\,\vec{\tau} - eA) - m - g_\sigma\sigma\right]\psi \\ & + \tfrac{1}{2}\left(\partial\sigma\right)^2 - \tfrac{1}{2}{m_\sigma}^2\sigma^2 - \tfrac{1}{4}\boldsymbol{\Omega}_{\mu\nu}\boldsymbol{\Omega}^{\mu\nu} + \tfrac{1}{2}m_\omega^2\omega^2 \\ & - \tfrac{1}{4}\vec{\boldsymbol{R}}_{\mu\nu}\vec{\boldsymbol{R}}^{\mu\nu} + \tfrac{1}{2}m_\rho^2\vec{\rho}^{\,2} - \tfrac{1}{4}\boldsymbol{F}_{\mu\nu}\boldsymbol{F}^{\mu\nu}\,, \end{aligned} \tag{1}$$

where m is the bare nucleon mass and ψ denotes the Dirac spinors. The masses m_σ, m_ω, and m_ρ are those of the σ meson, ω meson, and the ρ meson, with the corresponding coupling constants for the mesons to the nucleons as g_σ, g_ω, g_ρ, respectively, and e is the charge of the proton. These coupling constants and unknown meson masses are Lagrangian Eq. (1) parameters. Here, $\Omega^{\mu\nu}$, $\vec{R}^{\mu\nu}$, and $F^{\mu\nu}$ are the field tensors of the vector fields ω, ρ, and the photon.

This linear model has first been introduced by Walecka [106, 107], however, this simple model does not provide a quantitative description of nuclear system [108, 109] with interaction terms linear only in the meson fields. For a realistic description of complex nuclear system properties, a non-linear self-coupling

$$U(\sigma) = \tfrac{1}{2}m_\sigma^2\sigma^2 + \tfrac{1}{3}g_2\sigma^3 + \tfrac{1}{4}g_3\sigma^4 \tag{2}$$

for scalar mesons has turned out to be crucial [108]. In the meson-exchange model, the meson–nucleon vertex functions g_σ, g_ω and g_ρ are determined by adjusting the parameters of an assumed phenomenological density-dependence of meson–nucleon coupling to reproduce the experimental data in

finite nuclei. The couplings of the σ meson and ω meson to the nucleon field are defined as

$$g_i(\rho) = g_i(\rho_{\rm sat}) f_i(x) \quad \text{for} \quad i = \sigma, \omega\,, \tag{3}$$

where

$$f_i(x) = a_i \frac{1 + b_i(x + d_i)^2}{1 + c_i(x + d_i)^2} \tag{4}$$

is a function of $x = \rho/\rho_{\rm sat}$, and $\rho_{\rm sat}$ denotes the baryon density at saturation in symmetric nuclear matter. The eight real and positive parameters in Eq. (4) are not independent. In order to have small number of parameters in the fit, these eight parameters are constrained as follows [110]:

$$f_i(1) = 1\,, \qquad f_\sigma''(1) = f_\omega''(1)\,, \qquad f_i''(0) = 0\,. \tag{5}$$

The latter constraint guarantees that the rearrangement contributions becomes finite for zero density and do not diverge. These five constraints reduce the number of independent parameters to three. Three additional parameters in the isoscalar channel are $g_\sigma(\rho_{\rm sat})$, $g_\omega(\rho_{\rm sat})$, and m_σ. The functional form of the density dependence for the ρ-meson coupling is suggested by a Dirac–Brückner calculations of asymmetric nuclear matter

$$g_\rho(\rho) = g_\rho(\rho_{\rm sat}) \exp\left[-a_\rho(x-1)\right]\,. \tag{6}$$

The isovector channel is parameterized by $g_\rho(\rho_{\rm sat})$ and a_ρ. The eight independent parameters (seven coupling parameters and the mass of the σ meson) were adjusted to reproduce the properties of symmetric and asymmetric nuclear matter, and to ground state properties of spherical nuclei. The present investigation uses the very successful density-dependent meson-exchange DD-ME2 [89], and non-linear NL3* [91] parameter sets.

2.2. The point-coupling model

The effective Lagrangian density for the density-dependent point-coupling model [90, 111, 112] that includes the isoscalar–scalar, isoscalar–vector and isovector–vector four-fermion interactions is given by

$$\begin{aligned}
\mathcal{L} \;=\; & \bar\psi(i\gamma\,\partial - m)\psi \\
& -\frac{1}{2}\alpha_{\rm s}(\hat\rho)\left(\bar\psi\psi\right)\left(\bar\psi\psi\right) - \frac{1}{2}\alpha_V(\hat\rho)\left(\bar\psi\gamma^\mu\psi\right)\left(\bar\psi\gamma_\mu\psi\right) \\
& -\frac{1}{2}\alpha_{TV}(\hat\rho)\left(\bar\psi\vec\tau\gamma^\mu\psi\right)\left(\bar\psi\vec\tau\gamma_\mu\psi\right) \\
& -\frac{1}{2}\delta_S\left(\partial_v\bar\psi\psi\right)\left(\partial^v\bar\psi\psi\right) - e\bar\psi\gamma\cdot\boldsymbol{A}\frac{1-\tau_3}{2}\psi\,.
\end{aligned} \tag{7}$$

It contains the free-nucleon Lagrangian, the point-coupling interaction terms, and, in addition to these two, the model includes the coupling of the proton

to the electromagnetic field. The derivative terms in Eq. (7) account for the leading effects of finite-range interactions that are crucial for a quantitative description of the nuclear properties. The functional form of the chosen point-couplings is

$$\alpha_i(\rho) = a_i + (b_i + c_i x)\, e^{-d_i x}\,, \qquad (i = S, V, TV)\,, \tag{8}$$

where $x = \rho/\rho_{\rm sat}$, and $\rho_{\rm sat}$ denotes the nucleon density at saturation in symmetric nuclear matter. In the present work, we have used the recently developed density-dependent point-coupling interaction DD-PC1 [90].

In the present investigation, the axial and triaxail RHB with separable pairing is used [113–115]. In the presence of pairing, the single-particle density matrix is generalized to two densities [116]: the normal density $\hat{\rho}$ and the pairing tensor $\hat{\kappa}$. The RHB energy density functional is then given by

$$E_{\rm RHB}[\hat{\rho}, \hat{\kappa}] = E_{\rm RMF}[\hat{\rho}] + E_{\rm pair}[\hat{\kappa}]\,, \tag{9}$$

where $E_{\rm RMF}[\hat{\rho}]$ is given by

$$E_{\rm RMF}\left[\psi, \bar{\psi}, \sigma, \omega^{\mu}, \vec{\rho^{\mu}}, A^{\mu}\right] = \int {\rm d}^3 r \mathcal{H}\,, \tag{10}$$

and the $E_{\rm pair}[\hat{\kappa}]$ is given by

$$E_{\rm pair}[\hat{\kappa}] = \frac{1}{4} \sum_{n_1 n_1'} \sum_{n_2 n_2'} \kappa^{*}_{n_1 n_1'} \left\langle n_1 n_1' \right| V^{PP} \left| n_2 n_2' \right\rangle \kappa_{n_2 n_2'}\,. \tag{11}$$

n refers to the original basis, and $\langle n_1 n_1' | V^{PP} | n_2 n_2' \rangle$ are the matrix elements of the two-body pairing interaction. The effective interaction in the pp channel, in $\boldsymbol{r}$-space has the form of

$$V^{PP}\left(\boldsymbol{r_1}, \boldsymbol{r_2}, \boldsymbol{r_1'}, \boldsymbol{r_2'}\right) = -G\delta\left(\boldsymbol{R} - \boldsymbol{R'}\right) P(\boldsymbol{r})\, P(\boldsymbol{r'})\,, \tag{12}$$

where

$$\begin{aligned} \boldsymbol{R} &= \frac{1}{\sqrt{2}}\left(\boldsymbol{r_1} + \boldsymbol{r_2}\right)\,, \\ \boldsymbol{r} &= \frac{1}{\sqrt{2}}\left(\boldsymbol{r_1} - \boldsymbol{r_2}\right) \end{aligned} \tag{13}$$

are the center of mass and the relative coordinates, respectively. The form factor $P(\boldsymbol{r})$ is of the Gaussian shape

$$P(\boldsymbol{r}) = \frac{1}{\left(4\pi a^2\right)^{3/2}} e^{-r^2/2a^2}\,. \tag{14}$$

The two parameters $G = 728$ MeV fm^3 and $a = 0.644$ fm of this interaction are the same for the protons and neutrons. They are derived in Refs. [117–120] by mapping of the $^1S_0$ pairing gap of infinite nuclear matter to that of the Gogny-D1S force [121].

The constrained calculations are performed by imposing constraints on both axial and triaxial mass quadrupole moments. The potential energy surface (PES) studied as a function of the quadrupole deformation parameter is performed by the method of quadratic constrains [116]. The method of quadratic constraints uses an unrestricted variation of the function

$$\left\langle \hat{H} \right\rangle + \sum_{\mu=0,2} C_{2\mu} \left(\left\langle \hat{Q}_{2\mu} \right\rangle - q_{2\mu} \right)^2 , \tag{15}$$

where $\langle \hat{H} \rangle$ is the total energy, $\langle \hat{Q_{2\mu}} \rangle$ denotes the expectation values of mass quadrupole operators

$$\hat{Q}_{20} = 2z^2 - x^2 - y^2 \quad \text{and} \quad \hat{Q}_{22} = x^2 - y^2 , \tag{16}$$

$q_{2\mu}$ is the constrained value of the multipole moment, and $C_{2\mu}$ is the corresponding stiffness constant [116]. Moreover, the quadratic constraint adds an extra force term $\sum_{\mu=0,2} \lambda_\mu \hat{Q}_{2\mu}$ to the system, where

$$\lambda_\mu = 2C_{2\mu} \left(\left\langle \hat{Q}_{2\mu} \right\rangle - q_{2\mu} \right) \tag{17}$$

for a self-consistent solution. This term is necessary to force the system to a point in deformation space different from a stationary point. The augmented Lagrangian method [122] has also been implemented in order to resolve the problem of convergence of the self-consistent procedure which diverges while increasing the value of stiffness constant $C_{2\mu}$ used in the procedure.

3. Results and discussion

3.1. Potential energy surface

In Fig. 1, we display the calculated potential energy surfaces of even–even $^{178-220}$Pb isotopes as functions of the quadrupole deformation. It is done within the axially deformed RHB model with constrained quadrupole deformations. The spherical ground state is found in $^{178-184}$Pb and $^{202-220}$Pb nuclei, as expected for nuclei with proton shell closure at $Z = 82$. Beside these spherical ground states, several deformed (prolate and oblate) competing minima are also there at very low energy, corresponding to an evident shape coexistence in nuclei $^{182-200}$Pb. Furthermore, we can consider spherical ground states of nuclei $^{194-200}$Pb on the basis of larger external potential barrier as compared to their coexisting oblate minimum.

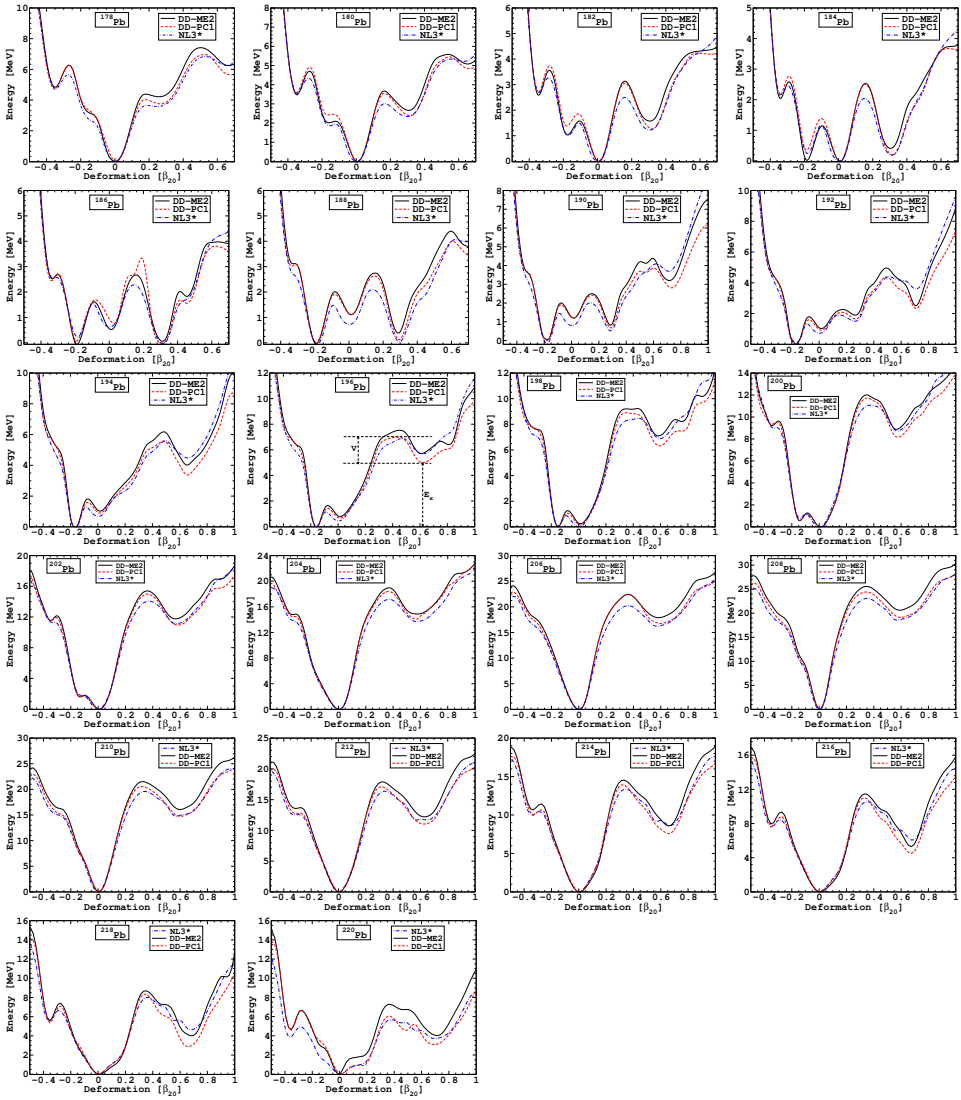

Fig. 1. Potential energy curves of even–even Pb isotopes from neutron number $N = 96$–138 as functions of the quadrupole deformation, obtained from axial RHB calculations with constrained quadrupole deformation. The effective interactions used are DD-ME2 (solid), DD-PC1 (dashed) and NL3* (dash-dotted). The curves are scaled such that the ground state has a zero MeV energy.

The nuclei $^{182-192}$Pb show triple-shape coexistence (oblate, prolate and spherical). Moreover, nuclei $^{184-190}$Pb have larger barrier potential between oblate, prolate and spherical minima as compared to nuclei ^{182,192}Pb. The

coexistence of triple-state in these nuclei is in qualitative agreement with the experimental finding [9, 13]. ^{182}Pb and ^{184}Pb have spherical ground states, in addition to low-lying oblate and prolate minima. The first 0^+ excited state in nuclei ^{182,184}Pb is oblate ($\beta_2 = -0.18$) and the second one is prolate ($\beta_2 = 0.30$). However, the ground state of ^{186}Pb is not spherical, rather prolate ($\beta_2 = -0.18$) with DD-PC1 and NL3*, and oblate ($\beta_2 = 0.31$) with DD-ME2. We find second minima as oblate ($\beta_2 = 0.31$) with DD-PC1 and NL3*, and prolate ($\beta_2 = -0.18$) with DD-ME2. Third minimum is spherical in the present calculation. The finding is the same for other ^{188,190,192}Pb isotopes having oblate, prolate and spherical shape as their first, second and third minima, respectively with all the effective interactions. However, on the basis of their external potential barrier heights, we can say that the triple-shape for these nuclei is prolate, oblate and spherical as their first, second and third minimum, respectively.

The structural evolution of Pb isotopes in terms of quadrupole moments is shown in Fig. 2. The encircled open square symbols indicate the shapes corresponding to the ground states obtained in our calculations. The ex-

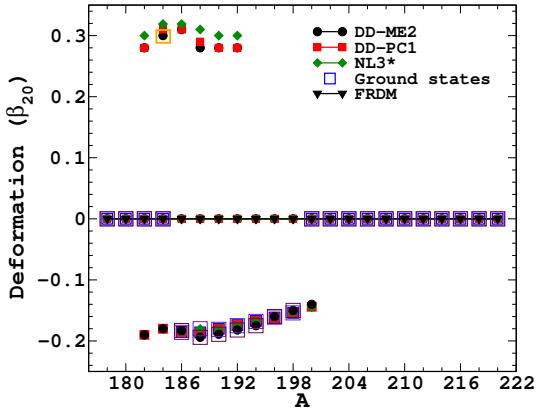

Fig. 2. (Color online) Quadrupole deformation parameters β_{20} for even–even Pb isotopes using DD-ME2, DD-PC1 and NL3* as a function of mass number (A), compared to FRDM values [99]. Results for prolate, oblate, and spherical minima are displayed with different symbols (see the legend). Ground state results are shown by open squares. In the case of ^{186}Pb, the ground state with DD-ME2 is shown by the gray/orange square.

citation energies of the three minima are compared with the experimental data [6, 9, 13, 19–29, 33, 34, 49, 50], shown in Fig. 3. We have plotted the excitation energies of the oblate and prolate minima relative to the spherical state. We notice that the crossing of the theoretical prolate and oblate states takes place at $A = 186$, as suggested by the experiment [9]. There is a partial agreement with the experimental excitation energies, but they

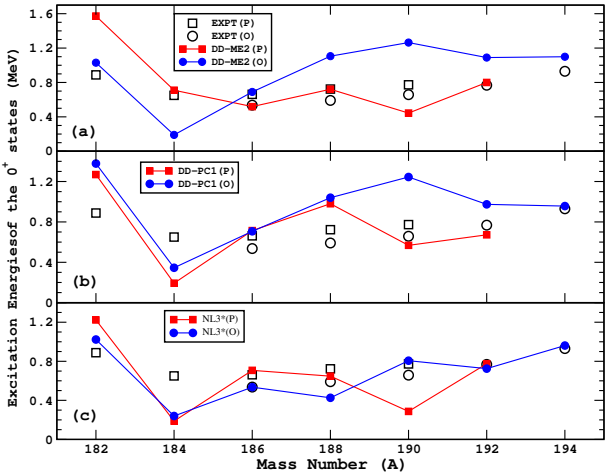

Fig. 3. Excitation energies of 0^+ excited states in $^{182-194}$Pb as a function of mass number (A). Compared to experimental (open symbols) excitation energies for the prolate (square) and oblate (circle) 0^+ states. Solid lines correspond to the axial RHB calculations with DD-ME2, DD-PC1, and NL3* effective interactions.

are not corresponding to their respective shapes. These results do reproduce quantitatively the experimental results, but also provide a good qualitative description of the triple-shape coexistence. So, we see that with an increasing neutron number, after $N = 184$, the oblate minimum is lowered in energy except at ^{186}Pb where it is prolate, and the nuclei $^{188-198}$Pb have oblate ground states, contradicting the experimental findings as ground state being of spherical shape. However, as discussed above, we can consider ground states of $^{194-200}$Pb nuclei as spherical ones. Further, with increasing neutron number, we find that $^{202-220}$Pb nuclei have spherical ground states.

Keeping in mind the role of the pairing correlations and the proton–neutron (p–n) interaction to interpret the low-lying prolate and oblate minima in the closed shell Pb isotopes [49, 50], we have shown the absolute values of the pairing energies for proton and neutron along with the potential energy curves (thick lines) for the isotopes $^{182-192}$Pb showing the triple-shape coexistence as the functions of the axially symmetric quadrupole moment with the DD-ME2, DD-PC1 and NL3* parameter set. We expect the proton pairing energy to vanish at and around the spherical shape because of the $Z = 82$ shell closure. This is what we get in Fig. 4. The neutron pairing energy is very large around the spherical shape. Further, for large deformation, the proton pairing energy increases and the neutron pairing energy decreases to the same extent. What else we notice is that apart from the zero of the proton pairing energy around the spherical shape, it also vanishes or approaches zero at other different deformations that is on either prolate or

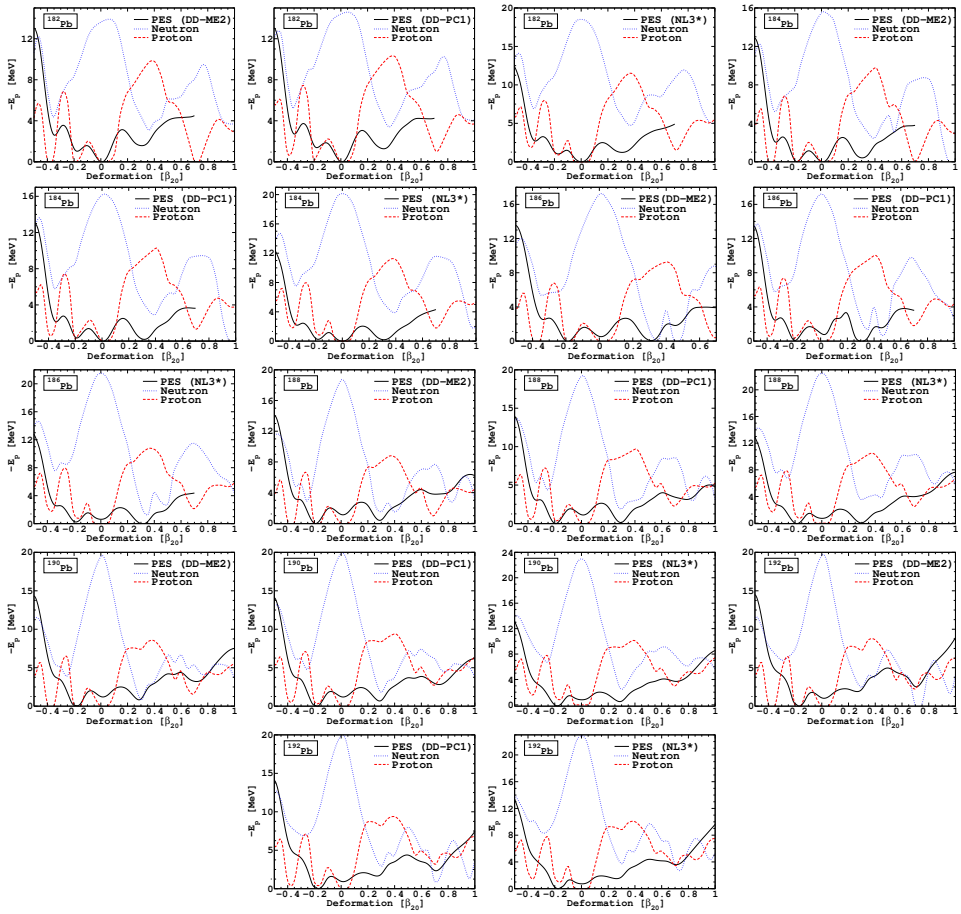

Fig. 4. (Color online) Mean field potential energy surfaces (continuous thick line) as well as the absolute value of the pairing energies for neutrons (dotted/blue line) and proton (dashed/red line) for the nuclei $^{182-192}$Pb considered as functions of the axially symmetric quadrupole moment with the DD-ME2, DD-PC1 and NL3* parameter set.

oblate side. The behavior of neutron and proton pairing energies is the same in almost all the isotopes with all the effective interactions considered. Earlier studies have shown that on the basis of the pairing energy contribution as well as the occupancies of the quasiparticle states in the single particle energies, one cannot predict directly the appearance of energy minima in the potential energy curve [49, 50].

In order to get a further insight into the triple-shape coexistence, we have performed the systematic constrained triaxial calculations for these $^{184-190}$Pb isotopes mapping the quadrupole deformation space defined by β_2 and γ using DD-ME2 and DD-PC1 effective interactions. For each nucleus, two contour plots have been made for each parameterization to investigate the location of a triaxial ground state, and the possibility of triple-shape coexistence. The location of the ground state in the β–γ deformation space is indicated by the point (β^0, γ^0). We can see in Fig. 5 the β–γ contour plots for $^{184-190}$Pb isotopes. We have also plotted the energy difference (ΔE) between the three minima as a function of β for fixed γ values. As can be

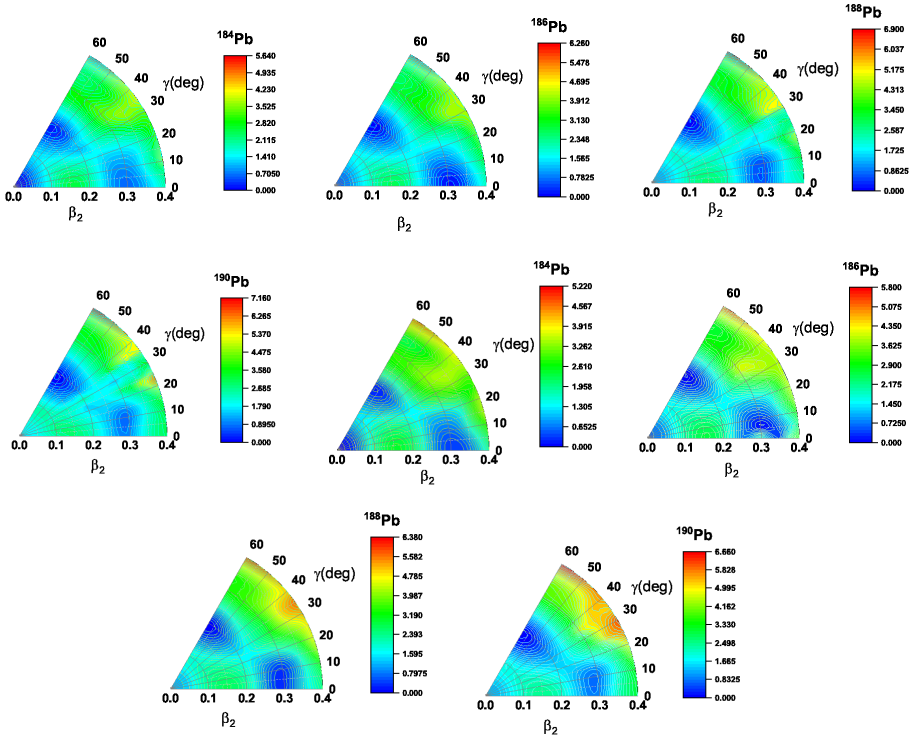

Fig. 5. (Color online) Mean field potential energy surfaces for the nuclei $^{184-190}$Pb in the (β, γ) plane, obtained from a triaxial RHB calculations with the DD-ME2 and DD-PC1 parameter set. The color scale shown at the right has the unit of MeV, and scaled such that the ground state has a zero MeV energy.

seen from Fig. 6, the triaxial calculations are confirming the coexistence of triple-shape with an energy difference of less than 1 MeV. In these figures, we can see that for ^{184}Pb, isotope the global minimum is spherical. Two of

the remaining minima are axially deformed oblate (0.236 MeV) and prolate (0.641 MeV). The axial prolate with an energy difference of 0.641 MeV agrees with the experimental prolate excitation energy of 0.65 MeV.

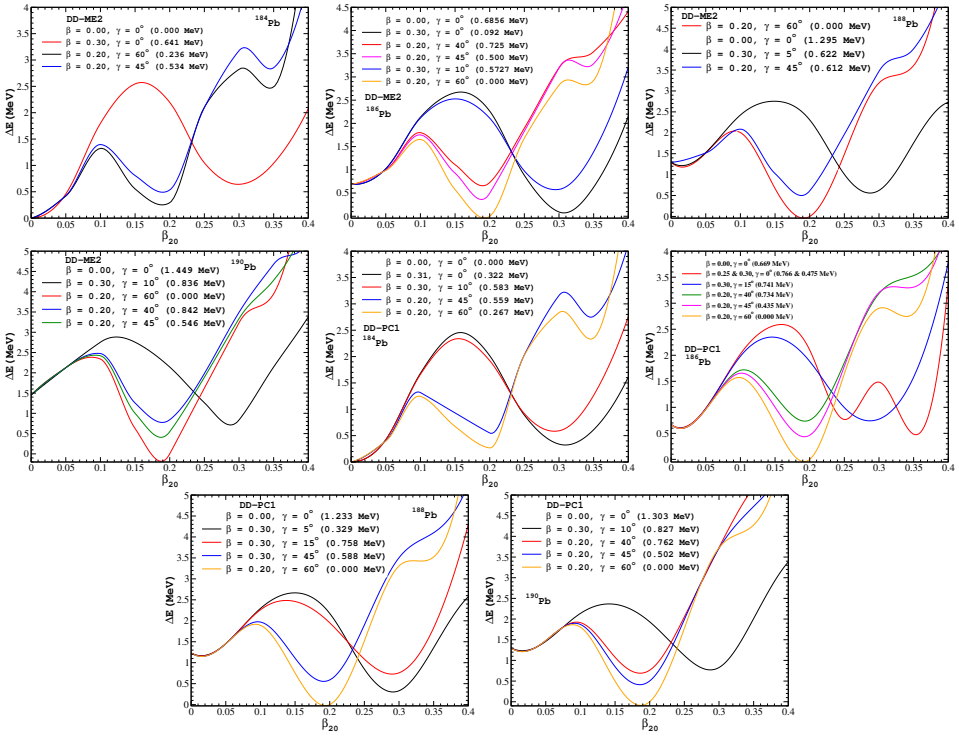

Fig. 6. Mean-field potential energy curves for the nuclei $^{184-190}$Pb showing the energy difference (ΔE) between the three minima as a function of β for fixed γ-values with DD-ME2 and DD-PC1 set.

For the ^{186}Pb isotope, the experimental ground state is spherical with two low-lying oblate (0.536 MeV) and oblate (0.662 MeV) minima. In our calculation, the global minimum is oblate at $\beta = 0.20$ and $\gamma = 60°$. The other two minima are spherical (0.686 MeV) and prolate (0.092 MeV). From Fig. 6, we can see that there is a competition between oblate (0.000 MeV) and prolate (0.092 MeV) to be the global minimum. Beside this, we have another axially prolate (0.573 MeV) minimum as well as triaxial minima with an energy difference of 0.725 MeV and 0.500 MeV closer to the experimental values. Further, in the case of ^{188}Pb and ^{190}Pb isotope, we observed the similar structures. The findings are almost the same with both the DD-ME2 and DD-PC1 parameterizations used. The comparison with experimental data [6, 9, 13, 19–29, 33, 34, 49, 50] is shown in Fig. 7.

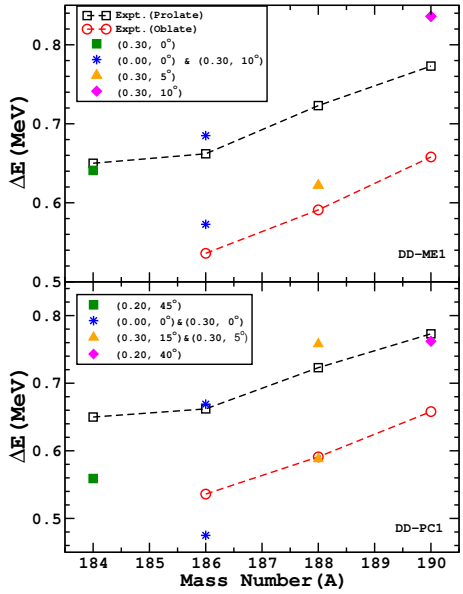

Fig. 7. Excitation energies of 0^+ excited states in $^{182-194}$Pb as a function of mass number (A) obtained in triaxial RHB calculations, compared to experimental (open symbols) excitation energies for the prolate (square) and oblate (circle) 0^+ states.

We see that the contradiction is there with the present RHB calculation and the experimental findings for those Pb isotopes in which the triple-shape coexistence is observed. We indeed are reproducing the triple-shape coexistence (spherical, prolate and oblate), but not as a spherical ground state along with the two low-lying prolate and oblate as first and second excited states, respectively, except for ^{184}Pb nuclei. This discrepancy may not be very significant. We can say that any tiny changes in the details of the calculations would lead to a different shape of the ground state due to very delicate competition between the spherical, axially prolate, oblate and triaxial shapes being within the very small degenerate energies.

3.2. Ground state properties

In Fig. 8, we display the binding energies per nucleon of even–even Pb isotopes, calculated within the RHB formalism using density-dependent zero and finite range mean-field effective nucleon–nucleon interactions DD-PC1, DD-ME2, respectively, and the non-linear finite range meson-exchange NL3* interaction, and with the separable pairing. In this figure, we have plotted those theoretical values that correspond to the ground states of the corresponding isotopes whether it is prolate oblate or spherical. The theoretical binding energies are compared with the available experimental data [97, 98].

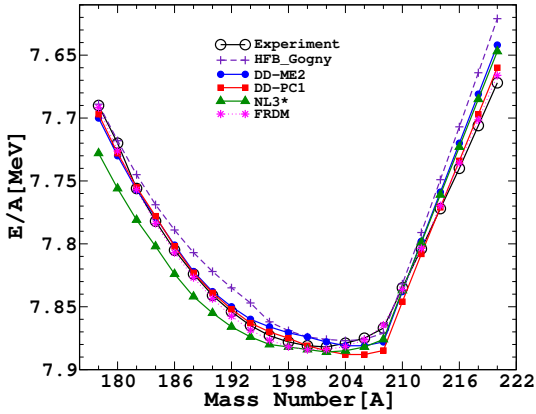

Fig. 8. Binding energies of even–even Pb isotopes calculated in the RHB model with the mean-field effective interactions DD-ME2, DD-PC1, and NL3*, and with the separable pairing model. The theoretical binding energies are compared with the experimental data [97, 98], FRDM [99], and HFB [100].

There is a good agreement with experimental data for both the density-dependent DD-ME2 and DD-PC1 interactions except they underbind the nuclei after ^{214}Pb, while the non-linear NL3* interaction strongly overbind the nuclei except around ^{208}Pb. The numerical results are also found to be in agreement with the Macro–microscopic FRDM calculations [99], and the self-consistent HFB calculations based on the interaction Gogny-D1S [100]. However, the HFB calculations underbind the nuclei throughout the isotopic series except around ^{208}Pb.

In Fig. 9, we can see the results obtained for S_{2n} energies for even–even Pb isotopes. The result is shown as a function of the even neutron number N in the range of interest. Focusing on the behavior, we see that besides the abrupt decrease of S_{2n} at $N = 126$ corresponding to the shell closure, the evolution of the S_{2n} along the isotopic chain shows a change in the tendency at $N = 104$ and at $N = 120$. This suggests a change in the ground-state shape of these isotopes corresponding to the transition from the spherical to the prolate, oblate and the spherical shape. In general, the measured S_{2n} are reproduced reasonably well using DD-ME2 and DD-PC1 interactions except underestimated by the calculations between $N = 120$ and $N = 138$ within 1–1.5 MeV. The numerical results with NL3* interaction underestimate the experimental data except in the region of $N = 126$ shell closure location. The calculated shell gap at $N = 126$ is larger than observed. Present numerical results are also found to be in agreement with the Macro–microscopic FRDM calculations [99], and the self-consistent HFB calculations based on the Gogny-D1S interaction [100] up to $N = 126$. After $N = 126$, it lies in between FRDM and HFB calculations.

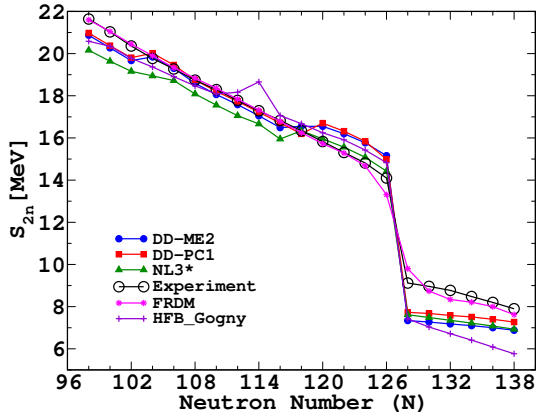

Fig. 9. Two neutron separation energies of even–even Pb isotopes calculated in the RHB model with the mean-field effective interactions DD-ME2, DD-PC1, and NL3*, and with the separable pairing model. The theoretical binding energies are compared with the experimental data [97, 98], FRDM [99], and HFB [100].

In Fig. 10, the experimental charge radii (solid circles) of Pb isotopes from [123] are compared against the predictions of the RHB calculations with DD-ME2, DD-PC1, and NL3* effective interactions with separable pairing. In these figures, we show the values for the oblate (down triangles), prolate (up triangles) and spherical (solid dots) shapes corresponding to the local minima in the potential energy curves. The theoretical values corresponding to the ground states of the isotopes are shown by open circles. We see the smooth increase of charge radii with a kink at $A = 208$ in the case of the spherical shape of Pb isotopes. We also observe that the lighter isotopes are spherical, then the shape changes to oblate at $A = 186$, remains oblate till $A = 196$, then becomes spherical. The observed jump at $A = 186$ and $A = 196$ corresponds to the transition from spherical to prolate. The charge radii corresponding to the prolate solution for the Pb isotopes are also shown. The oblate deformation appears near $\beta \sim -0.2$, while the prolate one appears around $\beta \sim 0.3$. In the case of DD-ME2, we get prolate deformation for the ground state. The behavior is similar to the one discussed and shown in the quadrupole deformation plot in Fig. 2. In contrast to this, the results of the calculations are in a good agreement with experimental data. The maximum deviation between the experimental values and the theoretical values corresponding to the ground state solution is 0.05 fm.

Figure 11 (a) shows the well-known anomalous kink in the isotopic shift of Pb isotopes, which represents the success of relativistic mean-field models in which it is expected to get naturally the anomalous charge isotopic shifts because of the intrinsic isospin dependence of the effective single-nucleon spin-orbit potential [124]. The numerical values of the mean-square nuclear

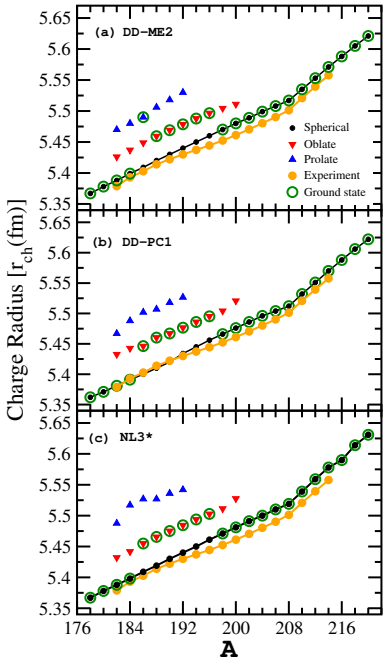

Fig. 10. Charge radii $r_{\rm ch}$ (fm) for even–even Pb isotopes using DD-ME2, DD-PC1 and NL3* as a function of mass number (A), compared to experimental data from Ref. [123]. Results for prolate, oblate, and spherical minima are displayed with different symbols (see the legend). Ground state results are shown by open circles.

charge radius used to calculate this isotopic shift correspond to the ground states (spherical, prolate or oblate) obtained in our calculations. The experimental values [125] of change in mean-square nuclear charge radius from optical isotopic shifts are very well reproduced in the present RHB calculation with DD-ME2, DD-PC1, and NL3* effective interactions with separable pairing. In Fig. 11 (b), we show the RHB calculations for the charge isotopic shift of even–even Pb isotopes compared with the experimental data [123]. The evolution of the nuclear charge radii relative to that of the $N = 126$ isotope, $\delta\langle {r_{\rm c}}^2\rangle = \langle {r_{\rm c}}^2\rangle^N - \langle {r_{\rm c}}^2\rangle^{126}$, is presented as a function of mass number. From the figure, we can see that the calculations follow nicely the measurements. There is a smooth increase of $\delta\langle {r_{\rm c}}^2\rangle$ up to $A = 206$, then a kink appears at $A = 208$ and the increase is smooth for heavier isotopes. The agreement improves substantially for heavier isotopes from $A = 194$.

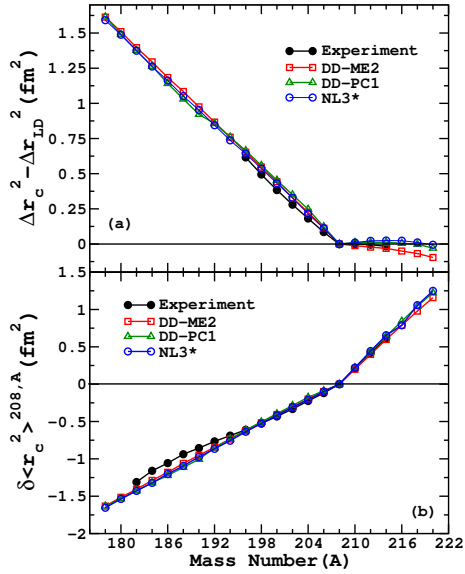

Fig. 11. Calculated charge isotopic shift in even–even Pb isotopes. The results of RHB calculations with the DD-ME2, DD-PC1, and NL3* effective interactions, and with the separable pairing, are compared with the experimental data from Refs. [123, 125].

3.3. Superdeformed states

In this section, we will report the systematic investigation of superdeformed (SD) states for even–even Pb isotopes in the axially constrained RHB framework for the interactions DD-ME2, DD-PC1, and NL3* with pairing treated by the separable model. The present RHB calculations show an excellent manifestation of this SD structure in Pb isotopes including the evolution of the excitation energy, depth of the well, deformation, and the comparison with the ND states.

Theoretical studies of Satula *et al.* [73] and Krieger *et al.* [74] dedicated to the properties of the SD states based on the nuclear potential energy surfaces have indicated that in the case of Pb isotopes, the stable SD minimum is expected at spin $I = 0$. These studies have also predicted that in the neutron-deficient Pb isotopes, nuclide with $N = 108$ will be the lightest Pb isotope in which a distinct SD minimum can be observed. They have predicted the depth of well to be 90 keV for ^{190}Pb. Further, Bender *et al.* [75] have suggested the well depth to be 1 MeV and deformation to be $\beta_2 \geq 0.7$ in his approach with Sly6 Skyrme interaction with a density-dependent zero range pairing force. But this deformation is much higher than the experimentally observed quadrupole moment $\beta_2 \sim 0.47$, and also with other theoretical model predictions. It is also suggested to search for SD states

in the $N = 106$ isotope ^{188}Pb. Experimentally [72], a superdeformed band has been observed in the most neutron-deficient isotope of Pb *i.e.* in the $N = 108$ isotope ^{190}Pb. Further, it is suggested that the excitation energy for SD band in ^{190}Pb may be similar to that of its neighboring nucleus ^{192}Pb.

In Fig. 1, we can see that in the present RHB calculations, the superdeformed (SD) states have started to appear from the ^{188}Pb nucleus except for NL3* parameter set. However, from ^{190}Pb onward, a clear SD minimum is there till ^{220}Pb for all the effective interactions. The excitation energy $E_{\rm SD}$ and the depth of well V of the SD minimum are calculated with respect to the ground state of the respective isotopes as shown in Fig. 1 for ^{196}Pb. We can see that it is difficult to observe the stable SD state for ^{188}Pb isotope in comparison to its neighboring ^{190}Pb nucleus. This is due to the significantly high-excitation energy relative to the ground of SD minimum with very stiff barrier. In Fig. 12, we are presenting the calculated excitation energies $E_{\rm SD}$ of Pb isotopes for SD minimum as the functions of neutron number, compared with the experimental data available [71]. For ^{188,190,192}Pb isotopes, the excitation energy decreases, and starts to increase with increasing neutron numbers from $N = 112$. It reaches a maximum at $N = 126$, then starts decreasing gradually approaching to a minimum. However, it is difficult to observe SD bands in Pb isotopes with $N > 118$, as the excitation energy is too high to approach these SD states. This fact is also reflected in the experimental observations, as why we observe SD states between $N = 110$ and $N = 116$. From Fig. 12, we observe that differ-

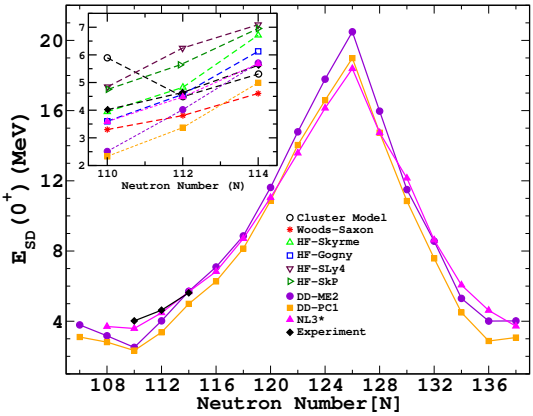

Fig. 12. Experimental and theoretical SD bandhead energies. Present results with the DD-ME2, DD-PC1, and NL3* effective interactions, and with the separable pairing, are compared with other model predictions and the experimental data [71] (insight of the figure). Strutinsky method using a Woods–Saxon potential [73]; HF-Skyrme, HF-SLy4, HF-SkP, and HF-Gogny: HFB using density-dependent Skyrme [74], SLy4 [76], SkP [76], and Gogny [77] interactions; cluster model [78].

ent theoretical approaches [73, 74, 76–78] including the present calculations reproduce the experimental finding of an increasing trend for the excitation energy with increasing neutron numbers. They are, however, not able to reproduce consistently the absolute energies as well as their differences. The present RHB calculation with NL3* parameterization does very well for all the three nuclei. Further, DD-ME2 parameterization reproduces it well for ^{192}Pb and ^{194}Pb, but, DD-PC1 underestimate except slightly for ^{196}Pb isotope.

If we look into the depth of the well given Table I, it follows almost the same trend as the excitation energy. This is an important parameter which affects the lifetime of the superdeformed states. There is a dip at $N = 112$ except with NL3*, and increase with the neutron number increase. It increases up to $N = 134$, but suddenly decreases at $N = 136$. Another fundamental property of the SD state is the quadrupole deformation parameter β_2, tabulated in Table II. It lies systematically between 0.6 and 0.7 for all the effective interactions. The finding agrees with the observation of superdeformed nuclei for excited states adopting ellipsoidal shapes with an axis ratio around 2:1 [60].

TABLE I

The depth of well of the superdeformed minimum V in the superdeformed states of $^{188-220}$Pb isotopes calculated with the DD-ME2, DD-PC1, and NL3* effective interactions.

Nuclei	DD-ME2	DD-PC1	NL3*
^{188}Pb	0.58	0.88	—
^{190}Pb	1.19	1.04	0.30
^{192}Pb	2.47	2.05	0.83
^{194}Pb	2.06	2.21	1.11
^{196}Pb	1.78	2.03	1.18
^{198}Pb	2.07	2.47	1.54
^{200}Pb	3.07	3.49	2.25
^{202}Pb	3.69	4.04	2.83
^{204}Pb	4.10	4.27	3.52
^{206}Pb	4.43	5.63	3.98
^{208}Pb	4.95	5.25	4.50
^{210}Pb	5.48	5.55	4.69
^{212}Pb	5.68	6.11	4.73
^{214}Pb	5.95	6.32	4.69
^{216}Pb	6.20	6.51	4.54
^{218}Pb	4.65	5.48	3.39
^{220}Pb	3.26	2.96	1.93

TABLE II

The quadruple deformation β_2 of the superdeformed states of $^{188-220}$Pb isotopes calculated with the DD-ME2, DD-PC1, and NL3* effective interactions.

Nuclei	DD-ME2	DD-PC1	NL3*
^{188}Pb	0.72	0.73	—
^{190}Pb	0.71	0.73	0.71
^{192}Pb	0.71	0.71	0.71
^{194}Pb	0.65	0.66	0.66
^{196}Pb	0.62	0.62	0.61
^{198}Pb	0.58	0.58	0.57
^{200}Pb	0.59	0.60	0.59
^{202}Pb	0.57	0.58	0.58
^{204}Pb	0.56	0.56	0.58
^{206}Pb	0.59	0.59	0.58
^{208}Pb	0.60	0.59	0.57
^{210}Pb	0.60	0.58	0.58
^{212}Pb	0.63	0.63	0.63
^{214}Pb	0.65	0.65	0.65
^{216}Pb	0.67	0.67	0.67
^{218}Pb	0.67	0.66	0.67
^{220}Pb	0.72	0.70	0.70

Figure 13 shows the binding energy per nucleon of the SD states, compared with the experimental SD energies [71]. There is a good agreement with experimental data for both the density-dependent DD-ME2 and DD-PC1 interactions. RHB with NL3* overestimate the experimental value for

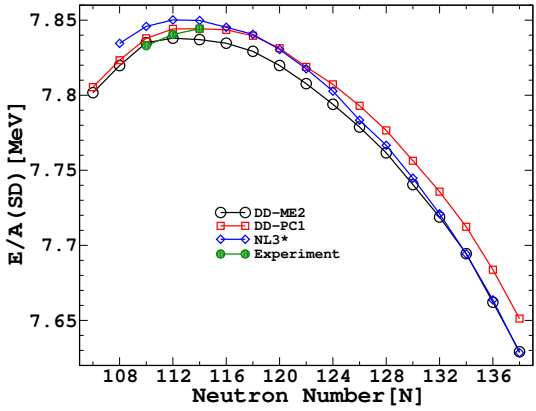

Fig. 13. Binding energy per nucleon for SD states, compared with the experimental data [71].

^{192,194}Pb isotopes. We can see that there is a jump at $N = 110$, and maximum appears at $N = 112$. This is in accordance with the suggestion made that $N = 112$ and $N = 114$ may appear as the semi-magic numbers at superdeformation [71].

In Fig. 14, we show two more sensitive parameters, two-neutron separation energy (S_{2n}) and its differential ΔS_{2n} for the superdeformed states. These are sensitive to the shell closure location within the isotopes. In Fig. 14 (a), agreement with the available data for $N = 112$ and $N = 114$ is quite good within 3–5%. Important are the prominent kinks appearing at $N = 110$, 118, 128, and 134. This can be more clearly seen in Fig. 14 (b). Peaks at $N = 110$ and 134 are more prominent in the DD-ME2 parameter set than DD-PC1 and NL3*. Two other peaks at $N = 118$ and $N = 128$ are equally present there with all the three effective interactions. It is known that the presence of the kinks and peaks in these analyses reflects the location of the shell closures. We can see that the presence of a peak or kink at $N = 110$ is nearer to the suggested semi-magic numbers ($N = 112$ or 114) at superdeformation [71]. Beside these, we also have candidates for semi-magic numbers $N = 118$, 128 and 134 at superdeformation. The present ΔS_{2n}

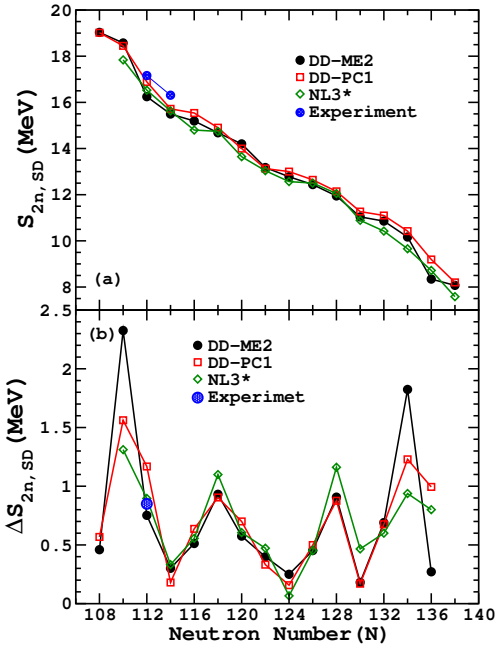

Fig. 14. (a) Two-neutron separation energy, (b) two-neutron separation energy difference in the superdeformation minimum obtained with DD-ME2, DD-PC1, and NL3* effective interactions, compared with the experimental data [63, 69, 71].

values for $N = 112$ agree very well with experiment (0.85 MeV) except with DD-PC1 which overestimate it by 300 keV. The DD-ME2 and NL3* differ in experimental value by 90 keV and 40 keV, respectively.

4. Conclusion

We have used the self-consistent mean-field model: the Relativistic Hartree–Bogoliubov (RHB) with density-dependent zero and finite range N–N interactions and separable pairing to perform a systematic calculation for the search of axial as well as triaxial ground state properties, triple-shape coexistence, and the structure of the superdeformed state of neutron-deficient Pb-isotopes $^{178-220}$Pb with neutron number $N = 96$–138.

In conclusion, we have found a reasonably good qualitative description of the experimental energies as well as the triple-shape coexistence (spherical, prolate and oblate) and their evolution with mass number. The discrepancy is not very significant because any tiny changes in the details of the calculations would lead to a different shape of the ground state due to very delicate competition between the spherical, axially prolate, oblate and triaxial shapes being within the very small degenerate energies. However, pairing fluctuations may play a role to improve the agreement with the experiment. We have shown that all the effective interactions consistently describe binding energies, charge radii, ground state quadrupole deformations and, at least qualitatively, the relative positions of coexisting minima in Pb isotopic chains. The different sensitivities of charge radii and $\delta\langle {r_c}^2\rangle$, indicate the structural changes, and more specifically, for shape transitions, changes in the behavior of the isotopic chains where the energies of the various shapes are almost degenerate. We know that beyond the mean field, the approach is appropriate for the quantitative analysis of shape coexistence, however, the present calculations within the relativistic mean-field model with the DD-ME2, DD-PC1 and, NL3* interactions in the *ph* channel, and with the separable pairing, reproduce in detail the empirical ground-state properties of neutron-deficient Pb isotopes.

Search for superdeformed states in $^{178-220}$Pb isotopes is investigated within the same framework. We have performed the projected potential energy surface (PES) calculations with axial symmetry for even–even Pb nuclei ($Z = 82$, $N = 96$ to 138). The present calculations clearly show the presence of superdeformed (SD) minima other than normal ground states for the Pb isotopes with neutron numbers $N = 106$ to 138. This is evident for all the effective interactions used. SD states start to appear at $N = 106$ ($A = 188$) which is earlier than the predicted $N = 108$ ($A = 190$). It is not there with the NL3* effective interaction. The numerical data for the excitation energy of the SD states are well-reproduced according to the trend predicted, *i.e.* the excitation energy increases with neutron number. In the present calculation, it reaches a maximum value at $N = 126$, then gradually

decreases approaching towards another minimum. A comparison with the predictions of other available models shows that no one correctly reproduces the excitation energies. However, present calculations with NL3* agree very well with experiment for $N = 112$ and 114, and with DD-ME2 for $N = 114$. The depth of well follows the increasing trend with neutron number with fluctuations at $N = 114$ and a sudden decrease at $N = 136$. The calculated quadrupole deformation in SD minima lies systemically between 0.6 and 0.7, which is consistent with the observation of experiment. The binding energy per nucleon for SD states is consistent with the standard trend, and agrees well with the experimental data available for $N = 110$, 112 and 114. At $N = 112$, we get its maximum. Two-neutron separation energies S_{2n} for SD states at $N = 112$ and 114 and its differential ΔS_{2n} for SD states at $N = 112$ are well-reproduced with kinks and peaks at $N = 110$, 118, 128, and 134. Systematics of the analysis indicates that $N = 112$ and $N = 114$ may appear as semi-magic numbers for superdeformation as suggested [71]. Other candidates for such semi-magic numbers for superdeformations may be $N = 118$, 128 and 134. In general, the separation energies for SD states are found to be significantly larger than the ground states (ND) of the respective isotopes, suggesting the lower level density at these SD states.

REFERENCES

[1] P. Cejnar, J. Jolie, R.F. Casten, *Rev. Mod. Phys.* **82**, 2155 (2010).

[2] K. Heyde *et al.*, *Phys. Rep.* **102**, 291 (1983).

[3] J.L. Wood *et al.*, *Phys. Rep.* **215**, 101 (1992).

[4] P. Federman, S. Pittel, *Phys. Lett. B* **69**, 385 (1977).

[5] K. Heyde, R.A. Meyer, *Phys. Rev. C* **37**, 2170 (1988).

[6] P. Van Duppen *et al.*, *Phys. Rev. Lett.* **52**, 1974 (1984).

[7] P. Van Duppen, M. Huyse, K. Heyde, J.L. Wood, *J. Phys. G* **16**, 441 (1990).

[8] K. Heyde, J. Schietse, C. De Coster, *Phys. Rev. C* **44**, 2216 (1991).

[9] R. Julin, K. Helariutta, M. Muikku, *J. Phys. G* **27**, R109 (2001).

[10] H. De Witte *et al.*, *Phys. Rev. Lett.* **98**, 112502 (2007).

[11] K. Heyde, J.L. Wood, *Rev. Mod. Phys.* **83**, 1467 (2011).

[12] P. Van Duppen, M. Huyse, *Hyperfine Interact.* **129**, 149 (2000).

[13] A.N. Andreyev *et al.*, *Nature (London)* **405**, 430 (2000).

[14] A. Dewald *et al.*, *Phys. Rev. C* **68**, 034314 (2003).

[15] K. Vyvey *et al.*, *Phys. Rev. C* **69**, 064318 (2004).

[16] M. Ionescu-Bujor *et al.*, *Phys. Rev. C* **81**, 024323 (2010).

[17] J. Bonn *et al.*, *Phys. Lett. B* **38**, 308 (1972).

[18] J. Bonn, G. Huber, H.-J. Kluge, E.W. Otten, *Z. Phys. A* **276**, 203 (1976).

[19] P. Van Duppen *et al.*, *Phys. Lett. B* **154**, 354 (1985).
[20] P. Van Duppen *et al.*, *Phys. Rev. C* **35**, 1861 (1987).
[21] J. Heese *et al.*, *Phys. Lett. B* **302**, 390 (1993).
[22] A.M. Baxter *et al.*, *Phys. Rev. C* **48**, R2140 (1993).
[23] J.F.C. Cocks *et al.*, *Eur. Phys. J. A* **3**, 17 (1998).
[24] D.G. Jenkins *et al.*, *Phys. Rev. C* **62**, 021302(R) (2000).
[25] T. Grahn *et al.*, *Eur. Phys. J. Special Topics* **150**, 121 (2007).
[26] G.D. Dracoulis *et al.*, *Phys. Lett. B* **432**, 37 (1998).
[27] G.D. Dracoulis *et al.*, *Phys. Rev. C* **60**, 014303 (1999).
[28] G.D. Dracoulis *et al.*, *Phys. Rev. C* **67**, 051301(R) (2003).
[29] G.D. Dracoulis *et al.*, *Phys. Rev. C* **69**, 054318 (2004).
[30] J. Pakarinen *et al.*, *Eur. Phys. J. A* **25**, 449 (2005).
[31] J. Pakarinen *et al.*, *Phys. Rev. C* **72**, 011304(R) (2005).
[32] J. Pakarinen *et al.*, *Phys. Rev. C* **75**, 014302 (2007).
[33] R.G. Allat *et al.*, *Phys. Lett. B* **437**, 29 (1998).
[34] P. Dendooven *et al.*, *Phys. Lett. B* **226**, 27 (1989).
[35] M.E. Estévez Aguado *et al.*, *Phys. Rev. C* **92**, 044321 (2015).
[36] N. Bijnens *et al.*, *Z. Phys. A* **356**, 3 (1996).
[37] J. Penninga *et al.*, *Nucl. Phys. A* **471**, 535 (1987).
[38] F.R. May, V.V. Paskevich, S. Frauendorf, *Phys. Lett. B* **68**, 113 (1977).
[39] R. Bengtsson *et al.*, *Phys. Lett. B* **183**, 1 (1987).
[40] R. Bengtsson, W. Nazarewicz, *Z. Phys. A* **334**, 269 (1989).
[41] W. Nazarewicz, *Phys. Lett. B* **305**, 195 (1993).
[42] N. Tajima *et al.*, *Nucl. Phys. A* **551**, 409 (1993).
[43] R.R. Chasman, J.L. Egido, L.M. Robledo, *Phys. Lett. B* **513**, 325 (2001).
[44] N.A. Smirnova, P.-H. Heenen, G. Neyens, *Phys. Lett. B* **569**, 151 (2003).
[45] T. Nikšić, D. Vretenar, P. Ring, G.A. Lalazissis, *Phys. Rev. C* **65**, 054320 (2002).
[46] T. Duguet, M. Bender, P. Bonche, P.-H. Heenen, *Phys. Lett. B* **559**, 201 (2003).
[47] M. Bender, P. Bonche, T. Duguet, P.-H. Heenen, *Phys. Rev. C* **69**, 064303 (2004).
[48] M. Bender, P.-H. Heenen, *J. Phys. G* **31**, 1611 (2005).
[49] R. Rodríguez-Guzmán, J.L. Egido, L.M. Robledo, *Phys. Rev. C* **69**, 054319 (2004).
[50] J.L. Egido *et al.*, *Phys. Rev. Lett.* **93**, 082502 (2004).
[51] J.M. Yao, M. Bender, P.-H. Heenen, *Phys. Rev. C* **87**, 034322 (2013).
[52] R. Fossion, K. Heyde, G. Thiamova, P. Van Isacker, *Phys. Rev. C* **67**, 024306 (2003).

[53] A. Frank, P. Van Isacker, C.E. Vargas, *Phys. Rev. C* **69**, 034323 (2004).
[54] K. Nomura, T. Otsuka, P. Van Isacker, *J. Phys. G* **43**, 024008 (2016).
[55] A. Frank, P. Van Isacker, C.E. Vargas, *Phys. Rev. C* **69**, 034323 (2004).
[56] O. Moreno, P. Sarriguren, R. Álvarez-Rodríguez, E. Moya de Guerra, *Phys. Rev. C* **73**, 54302 (2006).
[57] C.F. Jio, J.C. Pie, F.R. Xu, *Phys. Rev. C* **90**, 054314 (2014).
[58] C.F. Jio *et al.*, *Phys. Rev. C* **91**, 034309 (2015).
[59] C. Qi, L.Y. Jia, G.J. Fu, *Phys. Rev. C* **94**, 014312 (2016).
[60] B. Singh, R. Zywina, R.B. Firestone, *Nucl. Data Sheets* **97**, 241 (2002).
[61] T.L. Khoo *et al.*, *Phys. Rev. Lett.* **76**, 1583 (1996).
[62] G. Hackman *et al.*, *Phys. Rev. Lett.* **79**, 4100 (1997).
[63] A. Lopez-Martens *et al.*, *Phys. Lett. B* **380**, 18 (1996).
[64] K. Hauschild *et al.*, *Phys. Rev. C* **55**, 2819 (1997).
[65] A.N. Wilson *et al.*, *Phys. Rev. Lett.* **90**, 142501 (2003).
[66] S. Siem *et al.*, *Phys. Rev. C* **70**, 014303 (2004).
[67] E.F. Moore *et al.*, *Phys. Rev. Lett.* **63**, 360 (1989).
[68] B. Crowell *et al.*, *Phys. Rev. C* **51**, 1599(R) (1995).
[69] T. Lauritsen *et al.*, *Phys. Rev. C* **62**, 044316 (2000).
[70] M.S. Johnson *et al.*, *Phys. Rev. C* **71**, 044310 (2005).
[71] A.N. Wilson *et al.*, *Phys. Rev. Lett.* **95**, 182501 (2005).
[72] A.N. Wilson *et al.*, *Eur. Phys. J. A* **24**, 179 (2005).
[73] W. Satula *et al.*, *Nucl. Phys. A* **529**, 289 (1991).
[74] S.J. Krieger *et al.*, *Nucl. Phys. A* **542**, 43 (1992).
[75] M. Bender, P. Bonche, T. Duguet, P.-H. Heenen, *Phys. Rev. C* **69**, 064303 (2004).
[76] P.-H. Heenen, *et al.*, *Phys. Rev. C* **57**, 1719 (1998).
[77] J. Libert, M. Girod, J.-P. Delaroche, *Phys. Rev. C* **60**, 054301 (1999).
[78] G.G. Adamian, *et al.*, *Phys. Rev. C* **69**, 054310 (2004).
[79] B. Serot, J.D. Walecka, *Adv. Nucl. Phys.* **16**, 1 (1986).
[80] G.A. Lalazissis, P. Ring, *Phys. Lett. B* **427**, 225 (1998).
[81] Jian-You Guo, Zong-Qiang Sheng, Xiang-Zheng Fang, *Chin. Phys. C* **32**, 886 (2008).
[82] M.A. Riley, *et al.*, *Nucl. Phys. A* **512**, 178 (1990).
[83] B. Gall *et al.*, *Z. Phys. A* **348**, 183 (1994).
[84] A.V. Afanasjev, P. Ring, J. König, *Nucl. Phys. A* **676**, 196 (2000).
[85] S. Bouneau *et al.*, *Z. Phys. A* **358**, 179 (1997).
[86] T. Nakatsukasa, K. Matsuyanagi, S. Mizutori, Y.R. Shimizu, *Phys. Rev. C* **53**, 2213 (1996).

[87] R.R. Chasman, *Phys. Rev. Lett.* **80**, 4610 (1998).
[88] M.J. Joyce *et al.*, *Phys. Rev. Lett.* **71**, 2176 (1993).
[89] G.A. Lalazissis, T. Nikšić, D. Vretenar, P. Ring, *Phys. Rev.* **C71**, 024312 (2005).
[90] T. Nikšić, D. Vretenar, P. Ring, *Phys. Rev. C* **78**, 034318 (2008).
[91] G.A. Lalazissis *et al.*, *Phys. Lett. B* **671**, 36 (2009).
[92] S.E. Agbemava, A.V. Afanasjev, D. Ray, P. Ring, *Phys. Rev. C,* **89**, 054320 (2014).
[93] S.E. Agbemava, A.V. Afanasjev, D. Ray, P. Ring, *Phys. Rev. C,* **95**, 054324 (2017).
[94] A.V. Afanasjev S.E. Agbemava, *Phys. Rev. C* **93**, 054310 (2016).
[95] S.E. Agbemava, A.V. Afanasjev, T. Nakatsukasa, P. Ring, *Phys. Rev. C* **92**, 054310 (2015).
[96] T. Nikšić, N. Paar, D. Vretenar, P. Ring, *Comput. Phys. Commun.* **185**, 1808 (2014).
[97] Meng Wang *et al.*, *Chin. Phys. C* **41**, 030003 (2016).
[98] NUDAT database, National Nuclear Data Center, http://www.nndc.bnl.gov/nndc/nudat2/
[99] P. Möller, J.R. Nix, K.-L. Kratz, *At. Data Nucl. Data Tables* **66**, 131 (1997).
[100] J.-P. Delaroche *et al.*, *Phys. Rev. C* **81**, 014303 (2010); www-phynu.cea.fr/science_en_ligne/carte_potentiels_microscopiques/carte_potentiel_nucleaire_eng.htm
[101] H. Abusara, S. Ahmad, *Phys. Rev. C* **96**, 064303 (2017).
[102] H. Abusara, S. Ahmad, S. Othman, *Phys. Rev. C* **95**, 054302 (2017).
[103] Afaque Karim, S. Ahmad, *Phys. Rev. C* **92**, 064608 (2015).
[104] H. Abusara, A.V. Afanasjev, P. Ring, *Phys. Rev. C* **85**, 024314 (2012).
[105] Y.K. Gambhir, P. Ring, A. Thimet, *Ann. Phys. (NY)* **198**, 132 (1990).
[106] B.B. Serot J.D. Walecka, *Advances of Nuclear Physics*, edited by J.W. Negle, E. Vogt, Vol. 16, Planum, New York 1986.
[107] J.D. Walecka, *Ann. Phys. (NY)* **83**, 491 (1974).
[108] J. Boguta, A.R. Bodmer, *Nucl. Phys. A* **292**, 413 (1977).
[109] W. Pannert, P. Ring, J. Boguta, *Phys. Rev. Lett.* **59**, 2420 (1987).
[110] S. Typel, H.H. Wolter, *Nucl. Phys. A* **656**, 331 (1999).
[111] P.W. Zhao, Z.P. Li, J.M. Yao, J. Meng, *Phys. Rev. C* **82**, 054319 (2010).
[112] B.A. Nikolaus, T. Hoch, D.G. Madland, *Phys. Rev. C* **46**, 1757 (1992).
[113] W. Koepf, P. Ring, *Nucl. Phys.* **A493**, 61 (1989).
[114] T. Nikšić, N. Paar, D. Vretenar, P. Ring, *Comput. Phys. Commun.* **185**, 1808 (2014).
[115] P. Ring, *Prog. Part. Nucl. Phys.* **37**, 193 (1996).

[116] P. Ring, P. Schuck, *The Nuclear Many-Body Problem*, (Eds). W. Beiglbck *et al.*, New York, Springer-Verlag, 1980.

[117] Y. Tian, Z.Y. Ma, P. Ring, *Phys. Lett. B* **676**, 44 (2009).

[118] Y. Tian, Z.Y. Ma, P. Ring, *Phys. Rev. C* **79**, 064301 (2009).

[119] Y. Tian, Z.Y. Ma, P. Ring, *Phys. Rev. C* **80**, 024313 (2009).

[120] T. Nikšić *et al.*, *Phys. Rev. C* **81**, 054318 (2010).

[121] J.F. Berger, M. Girod, D. Gogny, *Comput. Phys. Commun.* **63**, 365 (1991).

[122] A. Staszczak, M. Stoitsov, A. Baran, W. Nazarewicz, *Eur. Phys. J. A* **46**, 85 (2010).

[123] I. Angeli, K.P. Marinova, *At. Data Nucl. Data Table* **99**, 69 (2013).

[124] M.M. Sharma, G.A. Lalazissis, P. Ring, *Phys. Lett. B* **317**, 9 (1993).

[125] P. Aufmuth, K. Heilig, A. Steudel, *At. Data Nucl. Data Tables* **37**, 455 (1987).